LIQUID-METAL DEVICES AND CIRCUITS FOR THERMAL APPLICATIONS AND COMMUNICATIONS

A THESIS SUBMITTED TO THE GRADUATE DIVISION OF THE UNIVERSITY OF HAWAIʻI AT MĀNOA IN PARTIAL FULFILLMENT OF THE REQUIREMENTS FOR THE DEGREE OF

MASTER OF SCIENCE

IN

ELECTRICAL ENGINEERING

MAY 2022

By

Saige J. Dacuycuy

Thesis Committee:

Wayne Shiroma, Chairperson

Aaron Ohta

Yao Zheng

ACKNOWLEDGMENTS

I would like to thank those who have helped me on my MS journey. I apologize in advance if I didn't mention anyone other than those listed here.

First, I would like to thank my advisor and friend, Dr. Wayne Shiroma, for being supportive of my professional and academic growth. I value the friendship that we've developed over our many walks. My favorite route to date is: "Out of Egypt and into the promised land, but after finally getting there it was gated." Thank you very much, and I look forward to continuing our walking routine, food adventures, and appreciation of Colorado during my PhD journey with you.

Second, I would like to thank my co-advisor and friend, Dr. Aaron Ohta, for challenging me to become better. I appreciate all of the guidance and support you gave me. I don't think I would have such fond interest in my research without you. I hope to share many fun memories and jokes with you during my PhD journey.

I would like to thank my examination committee for the constructive feedback on my thesis. To my third committee member, Dr. Yao Zheng, thank you for bringing enthusiasm and inspiration when imparting knowledge. I am glad to have you be a part of my thesis committee and I look forward to working with you more.

The work presented in this thesis was a valuable experience for me, and I wouldn't have done it without the support and ideas from those around me. I'd like to thank my lab mates over the past two years: Jon Itokazu and Tasmia Tahmid. I don't think I would have been who I am without you. I would also like to extend my thanks to all of the undergraduates that I had the pleasure to work with, specially: David Kimura, Nicholas Tom, Colby Kagamida, Ethan Mamuad, Jacob Marutani, and Glan Allan Manio. Special thanks to postdoctoral researcher, Dr. M Arif Rahman, for all the advice you gave me.

Finally, I would like to thank my loving family. You all have contributed to a part of my life, and I am thankful to you for providing me support. To my father, Rolando Dacuycuy, thank you for always being there for me when it matters most. My older brother, Detrick Dacuycuy, thank you for making me laugh and helping me find joy in life. My younger sister, Rayven Dacuycuy, thank you for sparking motivation in my life. And last but not least, I would like to thank my mother,

Sheree Dacuycuy. Thank you for helping me find my passion, providing endless love and support, and fighting for me to continue my dreams. I believe that all the work I have done up to this point was inspired by you. This is why you are the greatest mom in the world.

ABSTRACT

The unique properties of liquid metal, such as high electrical conductivity, high thermal conductivity, and deformability, offers promising opportunities for emerging devices and circuits. The focus of this thesis is on actuating liquid metal for potential applications in hot-spot cooling, sensing, and communications. First, continuous electrowetting of a liquid-metal droplet is demonstrated for controlled two-dimensional actuation and selective hot-spot cooling. In a 3 cm × 3 cm well, a Galinstan liquid-metal droplet could move at a terminal velocity of 13.3 cm/s with an actuation voltage of 11 V DC. For an actuation voltage of 10 V DC, the liquid-metal droplet decreases the temperature of a localized hot spot by approximately 7 °C. Next, controlled deformation of liquid metal by electrocapillary actuation is demonstrated in fluidic channels at the sub-millimeter-length scale. In 100-µm-deep channels of varying widths, the Galinstan liquid metal could move at velocities greater than 40 mm/s. The dynamic behavior and physical limitations of the liquid metal as it moves in the fluidic channels is described and is useful for designing microsystems that use liquid metal as a functional material.

TABLE OF CONTENTS

ACKNOWLEDGMENTS ii
ABSTRACT iv
LIST OF FIGURES vii
LIST OF ABBREVIATIONS ix
CHAPTER 1. INTRODUCTION 1
1.1 Thermal Management 1
1.2 Fabrication of Components at the Sub-Millimeter-Length Scale 2
1.3 Liquid-Metal Devices and Circuits 2
1.4 Thesis Organization 3
CHAPTER 2. TWO-DIMENSIONAL ACTUATION OF LIQUID-METAL DROPLETS FOR HOT-SPOT COOLING 4
2.1 Two-Dimensional Actuation 4
2.1.1 Experimental Setup 4
2.1.2 Results and Discussion 6
2.2 Hot-Spot Cooling 9
2.2.1 Experimental Setup 9
2.2.2 Thermal Effects of Applied Voltages 11
2.2.3 Hot-Spot Creation and Cooling 13
2.2.4 Effects of NaOH Electrolyte on Joule Heating 16
2.3 Conclusions 17
CHAPTER 3. ELECTROCAPILLARY ACTUATION OF LIQUID METAL IN MICROCHANNELS 19
3.1 Introduction 19
3.2 Materials and Methods 19
3.3 Concept 21
3.4 Results and Discussion 23
3.4.1 Elongation of Liquid Metal 23
3.4.2 Occupation Ratio 25
3.5 Conclusions 27
CHAPTER 4. CONCLUSIONS AND FUTURE WORK 29
4.1 Conclusions 29
4.2 Future Work 29
4.2.1 Higher Resolution at Hot-Spot Cooling 29

4.2.2 Continuous Pumping of Liquid-Metal Droplets for Hot-Spot Cooling 29
4.2.3 Further Investigation of Occupation Ratio 30
4.2.4 Improvements on Fabrication and Design 30
REFERENCES 32

LIST OF FIGURES

Figure 2.1 Layout of two-dimensional actuation device: (a) top view of 4-electrode device; (b) top view of 12-electrode device; (c) cross-sectional view of device well 6

Figure 2.2 Actuation of the liquid-metal droplet along a straight-line path for the (a)–(c) 4-electrode and (d)–(f) 12-electrode well 7

Figure 2.3 Droplet velocity as a function of voltage 8

Figure 2.4 Actuation of the liquid-metal droplet along an arbitrary path 9

Figure 2.5 Layout of 10-electrode device for hot-spot cooling 10

Figure 2.6 Demonstration of hot-spot cooling 11

Figure 2.7 (a) A region of interest was specified to measure the temperature at a 1 cm × 1 cm square in the upper-right corner of the NaOH well. (b) A temporal plot of ΔT for the region of interest 13

Figure 2.8 Time series of the device's heat map 14

Figure 2.9 Temporal plot of ΔT for the device's hot spot 15

Figure 2.10 Temporal plot of ΔT for the NaOH well with the liquid-metal droplet injected at the 150-s mark 16

Figure 2.11 A temporal plot of ΔT for various NaOH molarities 17

Figure 3.1 Layout of the microfluidic device for the electrocapillary actuation of liquid metal . 20

Figure 3.2 Electrocapillary actuation of liquid metal 21

Figure 3.3 Liquid metal extending into the primary channel through ECA 22

Figure 3.4 Demonstration of ECA for liquid metal in a 200-μm-wide channel 23

Figure 3.5 Average ECA velocity as a function of voltage 24

Figure 3.6 Maximum arm length as a function of voltage 25

Figure 3.7 The occupation ratio, or the ratio between the liquid-metal arm's thinnest width to its respective channel width ($w/w_0 \times 100\%$), as a function of the arm length 26

Figure 3.8 Measured ECA actuation velocities for an actuation voltage of 3 V DC 27

Figure 4.1 Concept of a liquid-metal bucket brigade 30

LIST OF ABBREVIATIONS

ECA: Electrocapillary actuation

CEW: Continuous electrowetting

PDMS: Polydimethylsiloxane

NaOH: Sodium hydroxide

CHAPTER 1. INTRODUCTION

The rapid improvements in computer performance have enabled researchers to pursue many scientific questions and obtain answers more accurately. For example, an electrical engineer can use a high-performance computer to design complex electronic products and obtain simulated electromagnetic results in a matter of seconds. To fulfill the requirements of a computer with fast processing speeds, billions of transistors must be incorporated into a single CPU chip [1]. As the CPU chips become smaller in size, the area to dissipate heat becomes smaller. This results in the heat being more concentrated and the chip heating up to elevated temperatures. The heat generated from the chip can result in shortened lifespan of the chip and lead to eventual failure of the computer [2]. Therefore, a method for the removal of heat is necessary.

In addition to the increased performance of computers, mobile communications have also improved every generation. Since the deployment of fifth generation (5G) systems, there has been an increased interest in beyond 5G, or sixth generation (6G) wireless systems [3]. Candidate technologies of 6G systems have higher data speeds, larger data capacity, and lower latency than 5G technology. To realize the benefits of 6G systems, which operates in the terahertz frequency range [4], 6G devices and its components need to be designed in the sub-millimeter-length scale.

1.1 Thermal Management

Removal of heat has become an ongoing issue in computer hardware. After 2010, a single CPU chip can dissipate more power per area than the surface of the sun [5]. Thus, to achieve maximum performance, the CPU chip must be properly cooled during operation.

Methods such as air cooling, liquid cooling [6], and thermoelectric cooling [7] have been used as a thermal management solution for electronics. Air cooling and liquid cooling are the two most used methods for CPU cooling. As for thermoelectric cooling, there has been slow progress in the materials research area [7]. Considering the increasing power density of CPU chips, it is necessary to research more innovative solutions to address electronic thermal management.

1.2 Fabrication of Components at the Sub-Millimeter-Length Scale

Fabricating metallic components at the sub-millimeter-scale has existed in fabrication technologies such as soft lithography [8] and inkjet printing [9]. For soft lithography, metallic structures can be deposited on elastomeric materials at the micrometer and nanometer scale. This technology is an attractive option for fabricating flexible electronics and biomedical devices. Inkjet printing offers a low-cost option for producing films of metal with precisely controlled thickness. Both soft lithography and inkjet printing are wonderful technologies for designing devices and components at the sub-millimeter level; however, once the metal is implemented onto a device it is difficult if not impossible to adjust the metal patterning after fabrication, making it difficult for devices that require reconfigurable elements.

1.3 Liquid-Metal Devices and Circuits

Considering the issues presented in electronic thermal management and wireless communications, there has been an increasing amount of interest in incorporating gallium-based liquid-metal alloys in devices and circuits. Gallium-based metal alloys such as eutectic gallium-indium and Galinstan are liquid at room temperature and exhibit high electrical conductivity, high thermal conductivity, and low toxicity [10–12]. These properties make it possible to integrate liquid metal into antennas [13–15], sensors [16,17], thermal management devices [18–20], actuation systems [21,22], electronics [23,24], thermoelectrics [25], plasmonics [26,27], and catalytic systems [28].

When an external electric potential gradient is applied to gallium-based liquid metal residing in an electrolytic solution, locomotive properties can also be realized [29], [30], making them useful for performing physical tasks when equipped with microtools [31]. Due to their precise positioning capability under low external electrical fields, liquid-metal droplets have recently shown promise for electronic thermal management [32].

Small volumes of liquid metal can also be used for developing 6G wireless systems. Due to the fluidic nature of liquid metal, it can be shaped to sizes smaller than a sub-millimeter-length scale while retaining its metallic properties. In addition to 6G wireless systems, liquid metals could find use in three-dimensional (3D) heterogeneous integration. The idea of 3D heterogeneous integration stacks distinct semiconductive materials and interconnects them vertically in a single package.

This type of packaging method offers multifunctionality on a single package. A key component of 3D heterogeneous integration is through-silicon vias (TSV), which are vertical interconnects between chips to create the 3D structures. TSVs have sub-millimeter diameters and are made of copper [33]. By substituting the copper in TSVs with liquid metal, it could help diversify the role of TSVs. Given its numerous properties and capabilities, liquid metal offers promising opportunities for emerging devices and circuits.

1.4 Thesis Organization

In this thesis, liquid metal is studied in two applications: electronic thermal management and microfluidics. The results presented in this work is beneficial for designing devices and circuits that use liquid metal as a functional material.

Chapter 2 presents research for using liquid-metal droplets in hot-spot thermal management. This approach utilizes continuous electrowetting (CEW) [34] to actuate a liquid-metal droplet within a two-dimensional path. Due to the high thermal conductivity of liquid metal, the droplet serves as a coolant substitute. By actuating the droplet to the location of the hot spot, the droplet absorbs some heat from the hot spot and effectively decreases the hot spot's temperature. With the dynamic movement of a liquid-metal droplet, selective hot-spot cooling can be achieved. Chapter 3 presents a characterization of liquid metal in channels at the sub-millimeter-length scale. Instead of moving the liquid metal from one location to another, the liquid metal is elongated into a channel through electrocapillary actuation (ECA) [35]. By observing the dynamics and physical limitations of the liquid metal in these confined channels, it will help in realizing applications that desire reconfigurable metallic elements in sub-millimeter lengths. The conclusion of this work, in addition to future research avenues, are presented in Chapter 4.

CHAPTER 2. TWO-DIMENSIONAL ACTUATION OF LIQUID-METAL DROPLETS FOR HOT-SPOT COOLING[1]

This chapter presents a hot-spot cooling technique in which a liquid-metal droplet is actuated toward an arbitrarily located hot spot, then actuated away from that hot spot to facilitate rapid cooling. Actuation is achieved via continuous electrowetting CEW [34], in which a voltage is applied to a non-toxic, room-temperature, liquid-metal alloy Galinstan droplet residing in a solution of sodium hydroxide (NaOH) [36]. The droplet moves along arbitrarily prescribed trajectories in an open two-dimensional plane, with electrodes embedded in the walls of a polydimethylsiloxane (PDMS) well.

The only known previous work using a CEW-based liquid-metal droplet cooling system is [20], in which the droplet transports heat away from a hot spot within a closed-loop channel; however, this limits the hot spot to a fixed location along that closed loop. This chapter demonstrates a method for selectively choosing the location of the hot spot and heat sink within a two-dimensional plane. With the generation of a hot spot, we demonstrate electrical actuation of a liquid-metal droplet along arbitrarily prescribed trajectories for selective hot-spot cooling.

2.1 Two-Dimensional Actuation

2.1.1 Experimental Setup

To demonstrate the actuation of liquid-metal droplets in 2D, a well with integrated electrodes was fabricated (Figure 2.1). A 3 cm × 3 cm × 0.8 cm well was cut into a layer of PDMS that was bonded on a flat piece of polystyrene. The well is filled with 1-M NaOH and contains a Galinstan liquid-metal droplet with a volume of approximately 0.07 ml. Nickel strips serve as the electrodes of the well and are embedded into the PDMS walls by transfixing nickel rods into the electrodes and the PDMS. Voltages applied to these electrodes are used for CEW actuation. The applied voltages create surface-tension gradients and Marangoni forces at and near the surface of the liquid-metal droplet, causing it to move. Thus, to actuate the liquid-metal droplet, a voltage is applied

[1] The work presented in this chapter is based on: S. J. Dacuycuy, W. A. Shiroma, and A. T. Ohta, "Two-dimensional actuation of liquid-metal droplets for hot-spot cooling," in *Proc. IEEE Intersociety Conf. Therm. and Thermomech. Phenom. Electron. Syst. (iTherm)*, Jun. 2021, pp. 1262–1267 [18].

to a single electrode while grounding the other electrodes. The droplet moves toward the higher-voltage electrode. To reverse the direction of motion, the voltage polarity on the electrodes is switched.

(a)

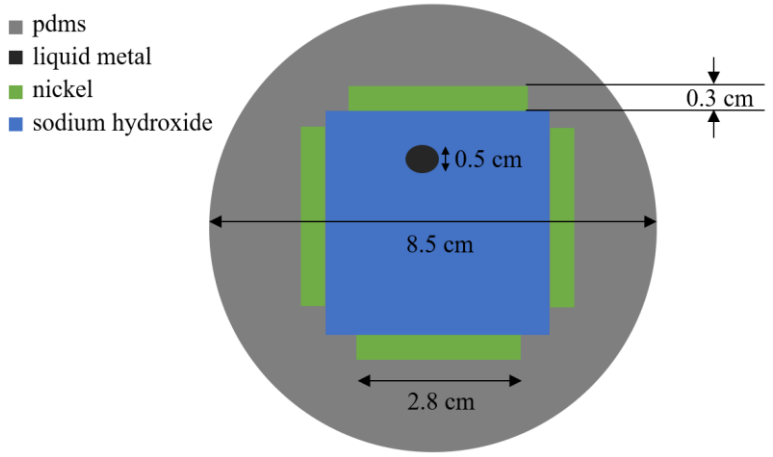

(b)

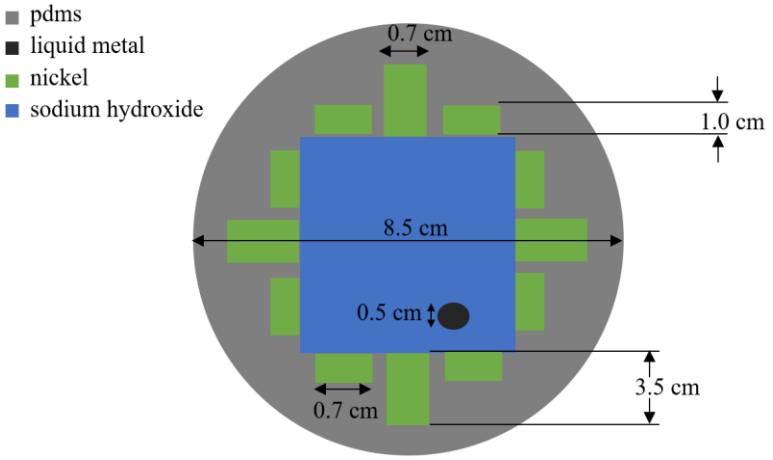

(c)

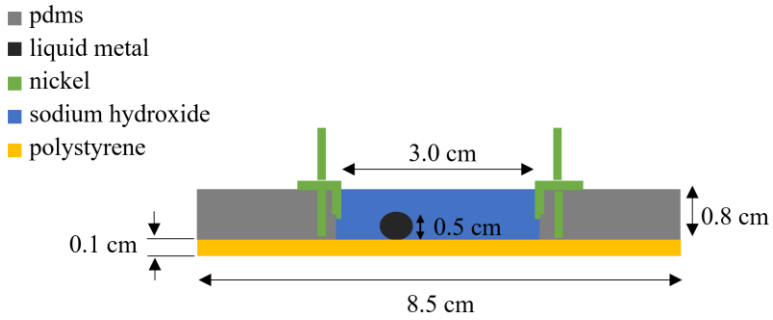

Figure 2.1 Layout of two-dimensional actuation device: (a) top view of 4-electrode device; (b) top view of 12-electrode device; (c) cross-sectional view of device well.

Two identical wells were constructed with different electrode placements. The 4-electrode well used four nickel strips as the electrodes, each 2.8 cm long. The 12-electrode well used 12 nickel strips, each 0.7 cm long.

An Arduino Mega ADK was used to control the electrode voltages. For the 4-electrode well, one STMicroelectronics L298N dual H-bridge motor driver was used to move the droplet in cardinal directions. For the 12-electrode well, three L298N motor drivers were used to move the droplet in both cardinal and intercardinal directions.

A Sony HDR-CX580V camera mounted on a tripod recorded the movement of the droplet. The droplet velocity from electrode to electrode was determined with an open-source software, *Tracker*, by measuring the position of the droplet between the video frame rates [37].

2.1.2 Results and Discussion

Figure 2.2 shows the actuation of the droplet in a 4-electrode well and 12-electrode well. In both cases, the droplet moved from the left electrode to the right electrode in a straight path.

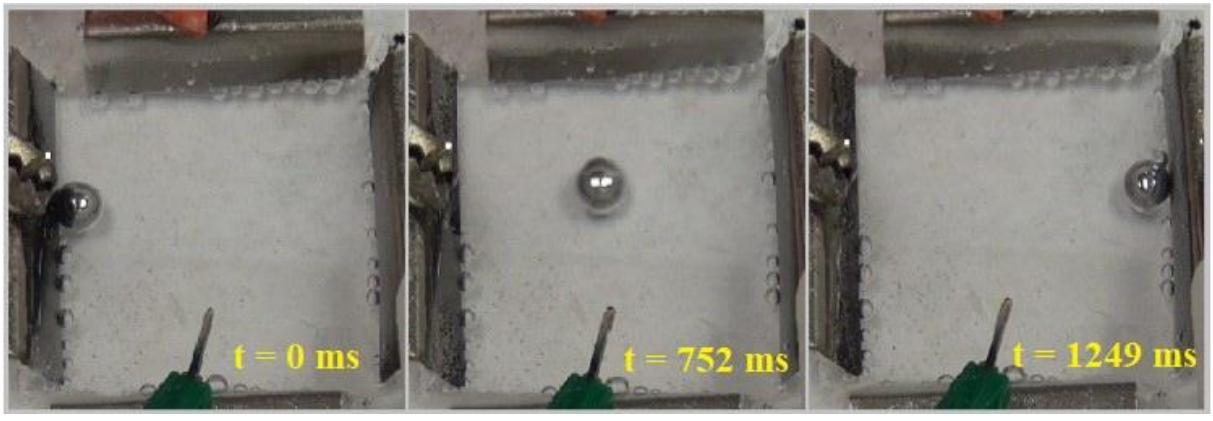

(a) (b) (c)

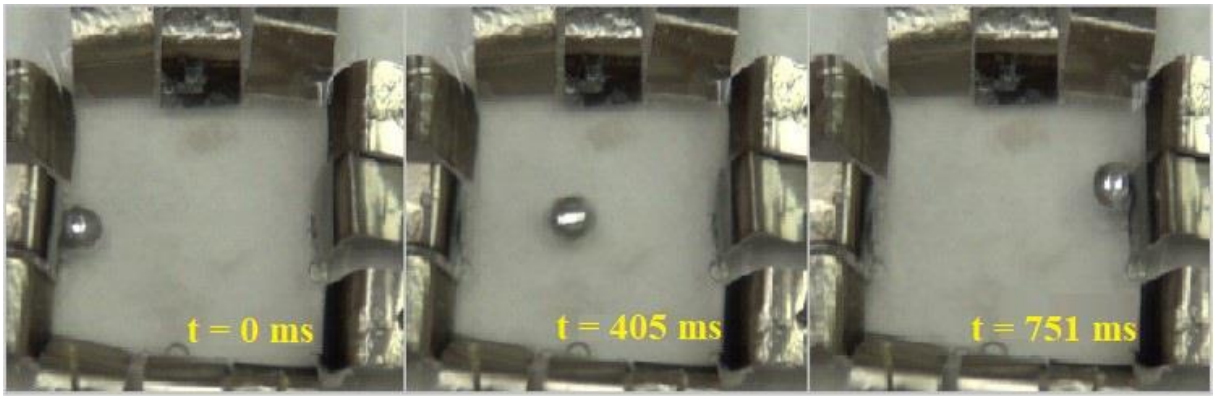

(d) (e) (f)

Figure 2.2 Actuation of the liquid-metal droplet along a straight-line path for the (a)–(c) 4-electrode and (d)–(f) 12-electrode well. From left to right: starting electrode, middle of the well, and opposite electrode. In all cases, the actuation voltage is 7.5 V DC.

Figure 2.3 shows the droplet's maximum velocity as a function of voltage. The droplets reached a 13.3-cm/s terminal velocity at approximately 11 V DC, suggesting that the actuation process for

the device does not require an actuation voltage greater than 11 V DC. If the droplet travels at a maximum velocity of 13.3-cm/s, then the droplet can travel across the entire well within 1 second.

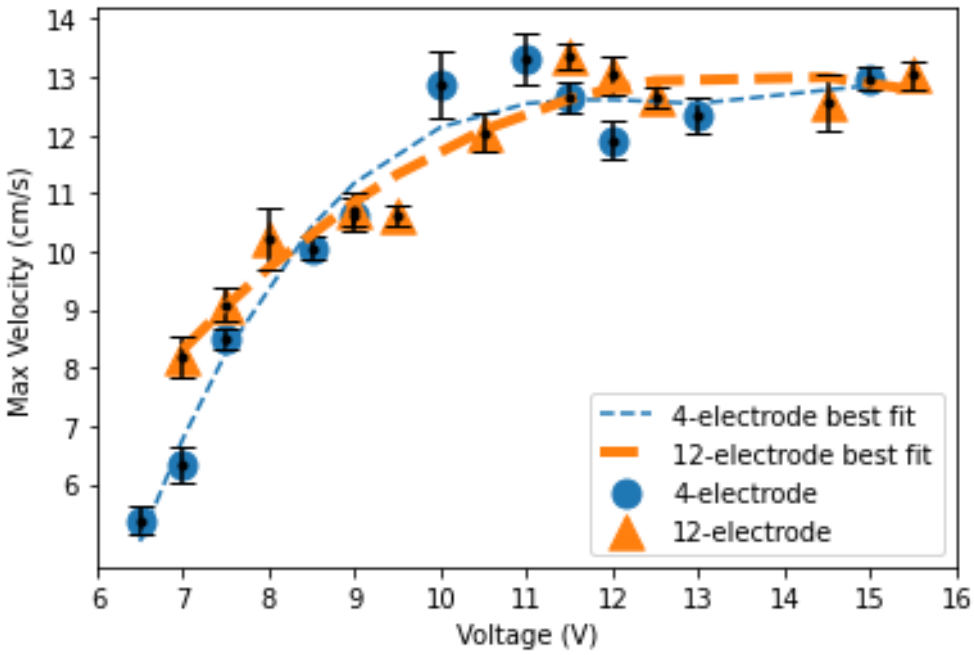

Figure 2.3 Droplet velocity as a function of voltage.

In addition to the droplet moving in a straight path, as shown in Figure 2.2, the droplet can move along an arbitrary path (Figure 2.4). To achieve this, a potential of 11 V DC was first applied to Electrode 2 while Electrode 1 was grounded. After the droplet moved to the desired position near Electrode 2, Electrodes 1 and 2 were grounded, and 11 V DC was applied to Electrode 3. It was only possible to move the droplet along a path like this using the 12-electrode well, so increasing the number of electrodes increases the precision of motion of the droplet. Applying voltages

sequentially can change the droplet's trajectory. By selectively choosing which electrodes to attract the droplet, more complex paths can be realized.

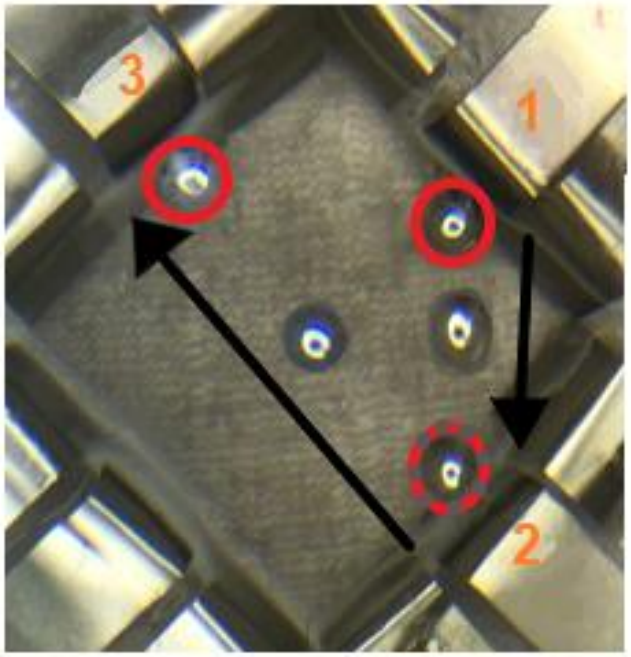

Figure 2.4 Actuation of the liquid-metal droplet along an arbitrary path. The desired path is indicated by the black arrows and the droplets outlined in red are the initial and final positions of the traveling droplet. The red dashed circle is the position of the droplet midway through the actuation sequence. The potential difference between the actuating electrode pairs was 11 V DC. The electrodes used in this actuation sequence are numbered for reference.

2.2 Hot-Spot Cooling

2.2.1 Experimental Setup

For this experiment, the 12-electrode well configuration given in Figure 2.1(a) was modified by using stainless steel electrodes and merging the top-right electrodes and the bottom-left electrodes (Figure 2.5). The enlarged electrode geometry covers opposite corners of the PDMS well, and serves multiple purposes. The top-right electrode is used to generate a localized hot spot, and the bottom-left electrode serves as a rudimentary heat sink. At the same time, the top-right and bottom-left electrodes can still be used for CEW actuation. The larger area of the top-right and bottom-left electrodes help with imaging of the temperature in the system using an infrared camera; however, it is possible to achieve similar results with the original 12-electrode configuration as well.

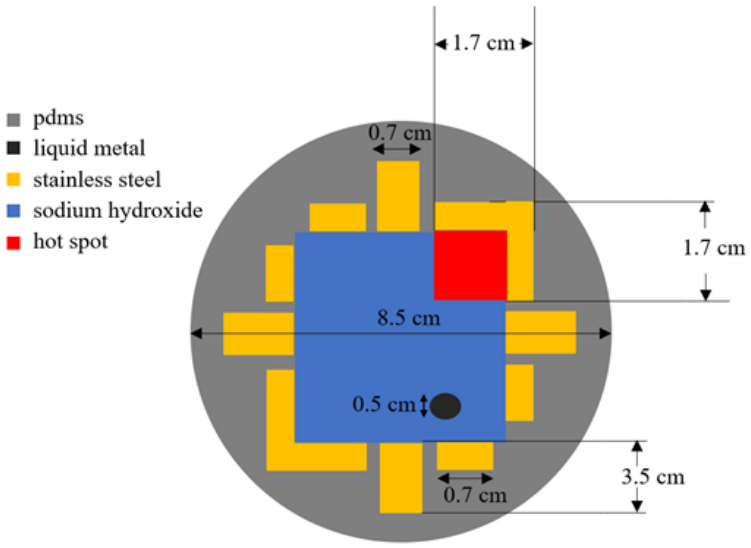

Figure 2.5 Layout of 10-electrode device for hot-spot cooling. The red region in the well is the hot spot generated by applying a voltage to the top-right electrode, which in turn heats up a section of the NaOH.

To demonstrate the concept of Figure 2.5, a hot spot is created then cooled once the liquid-metal droplet is injected and actuated to the hot spot (Figure 2.6). The well is first filled with 1-M NaOH, and a positive voltage is then applied to the top-right electrode for a period of 165 s. During this period, the applied voltage heats up the NaOH, creating a hot spot near the top-right electrode [Figure 2.6(a)]. After 150 s of electrode activation, a liquid-metal droplet is manually injected by a syringe into the middle of the well. The droplet moves toward the top-right electrode via CEW within 1 second, and cools the hot spot [Figures 2.6(b)–(c)]. The droplet occupies the hot spot for approximately 10 s, then the polarity is switched between the top-right electrode and the bottom-left electrode, and the droplet moves in the direction of the bottom-left electrode, which serves as a rudimentary heat sink. The droplet takes approximately 1 second to move from the top right to the bottom left, and is kept in contact with the heat sink for the remainder of the experiment [Figure 2.6(d)].

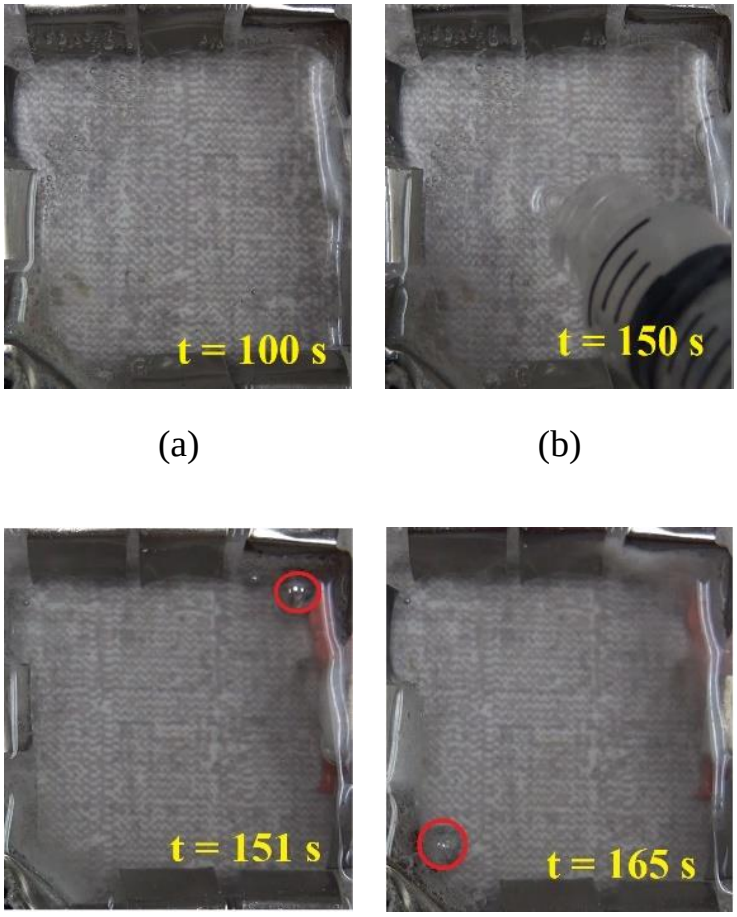

Figure 2.6 Demonstration of hot-spot cooling. (a) NaOH well when voltage has been applied for 100 s. During this time period, the hot spot is generated in the NaOH near the top-right electrode by Joule heating. The total duration of activation of the top-right electrode is 165 s. (b) At the 150-s mark, the liquid-metal droplet is injected at the center of the NaOH well using a syringe (visible in this photo). The liquid-metal droplet moves toward the top-right by CEW, and reaches the hot spot within 1 s. (c) At the 151-s mark, the droplet is at the hot spot. The droplet remains in this location for ~ 10 s, then (d) the polarity of the signal is switched so that the droplet moves via CEW toward the bottom-left electrode, which serves as the heatsink. The droplet reaches the heat sink within 1 s. Once the droplet reaches the heat sink, it remains in contact with the heat sink until the experiment is terminated at 170 s. The location of the liquid-metal droplet is outlined in red in the photos.

2.2.2 Thermal Effects of Applied Voltages

An experiment was conducted to measure the Joule heating of the NaOH caused by the CEW actuation voltages. To isolate this effect, no liquid metal was in the PDMS well. The temperature

was measured at the top-right corner of the well when a voltage of 10 V DC or 11 V DC was applied to the top-right electrode while the other electrodes were grounded (Figure 2.7). For the 2D actuation discussed in Section 2.1.2, the CEW voltages are applied for less than 1 s; thus, to quantify the Joule heating, the temperature was measured for a period of 10 s [Figure 2.7(b)] to show that the applied voltage does not cause any appreciable heating in the actuation time window.

A FLIR SC6xx series infrared camera mounted on a tripod recorded the heat map of the device. The *ResearchIR* software, compatible with the camera, is used to extract temperature data from the recorded video. The temperature data was also measured and verified using an OMEGA thermometer with an OMEGA Type K thermocouple.

(a)

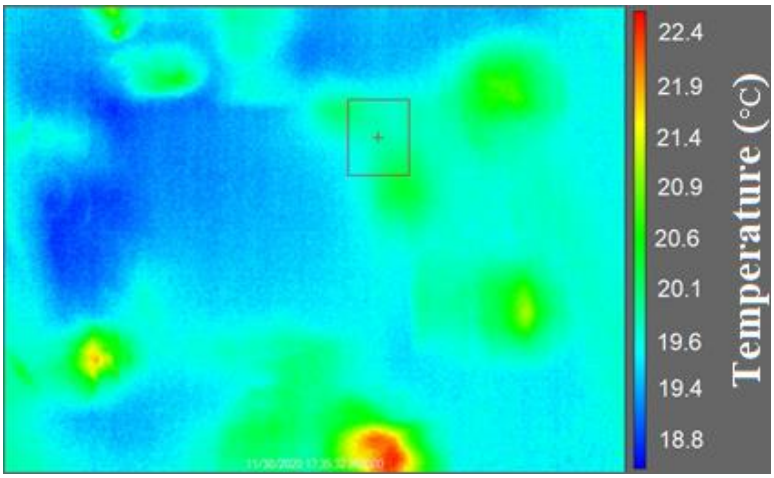

(b)

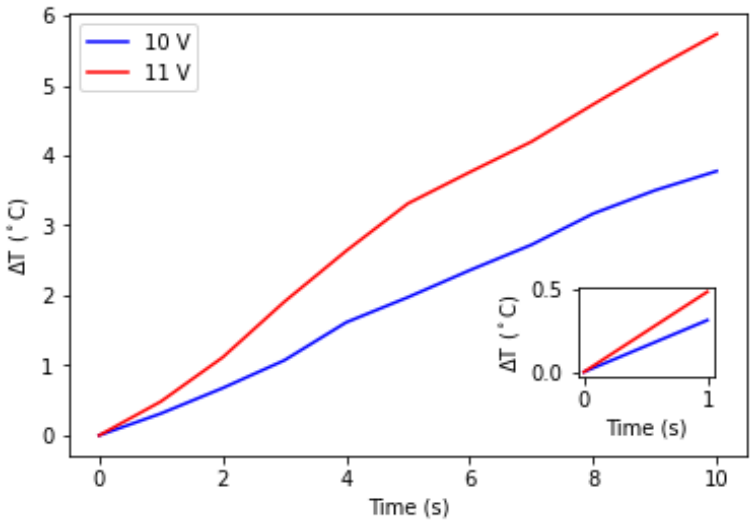

Figure 2.7 (a) A region of interest was specified to measure the temperature at a 1 cm × 1 cm square in the upper-right corner of the NaOH well. (b) A temporal plot of ΔT for the region of interest. The inset represents the actuation time window.

The heating caused by the activation of the top-right electrode was distributed throughout the region of interest (a 1 cm × 1 cm area in the top-right corner of the PDMS well) by the NaOH [Figure 2.7(a)]. The applied voltage causes the temperature of the NaOH to slowly increase [Figure 2.7(b)] at a rate of 0.39 °C/s for a 10-V signal, and 0.58 °C/s for an 11-V DC signal. The inset of Figure 2.7(b) shows that the temperature increase is less than 0.5 °C over the duration of a typical CEW actuation signal.

2.2.3 Hot-Spot Creation and Cooling

As a baseline for investigating the effectiveness of liquid-metal-droplet hot-spot cooling, the process described in Figure 2.6 was conducted without a liquid-metal droplet. In the absence of injecting a liquid-metal droplet into the device well, the Joule heating of NaOH continues to increase beyond the 150-s mark of electrode activation. Temperature measurements are taken for three time points with and without the liquid-metal droplet: before the voltage was applied (t = 0 s), after the voltage has been applied for 150 s, and after the voltage has been applied for 160 s (Figure 2.8). The experiment was carried out for applied voltages of 10 V DC and 11 V DC.

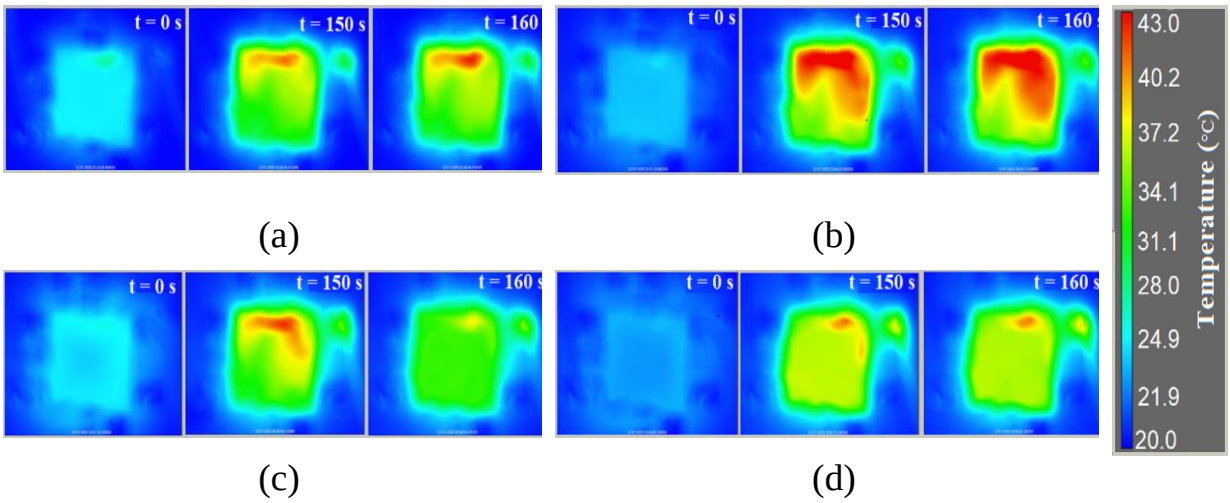

Figure 2.8 Time series of the device's heat map. The top row is without liquid metal at (a) 10 V DC and (b) 11 V DC. In the bottom row, a liquid-metal droplet is injected at 150 s with an actuation voltage of (c) 10 V DC and (d) 11 V DC.

Compared to the heat map for Joule heating at 10 V DC [Figure 2.8(a)], there is a significant distribution of heat throughout the NaOH well at an applied voltage of 11 V DC [Figure 2.8(b)]. The heat maps verify the results in Figure 2.7(b), in which the NaOH temperature increases at a faster rate for higher voltage.

The liquid-metal droplet is manually injected at the 150-s mark. After approximately 10 s of the droplet occupying the hot spot (t = 160 s), a decrease in temperature of approximately 3 °C was achieved at the hot spot for an actuation voltage of 10 V DC [Figure 2.8(c)]. For an actuation voltage of 11 V DC, a decrease in temperature of approximately 3 °C was observed at t = 160 s [Figure 2.8(d)]. The cooling effect of the liquid-metal droplet at the hot spot competes with the continued Joule heating of the NaOH.

The change in hot-spot temperature for the 10 V DC and 11 V DC actuation voltages is shown in Figure 2.9. Each data point represents the average of four separate trials. At approximately t = 151 s there is a 7 °C temperature drop at the hot spot for an actuation voltage of 10 V DC. This suggests that the liquid metal is providing rapid cooling at the hot spot.

At approximately t = 151 s, the liquid-metal droplet occupies the hot spot for approximately 10 s and then moves toward the heat sink. The reason for the rise in temperature after the rapid cooling is most likely due to the liquid-metal cooling competing with sustained heat from the activated electrode. The decreasing trend between the 150-s and 175-s marks could be contributed to the hot-spot electrode not being activated when the droplet moves toward the heat sink.

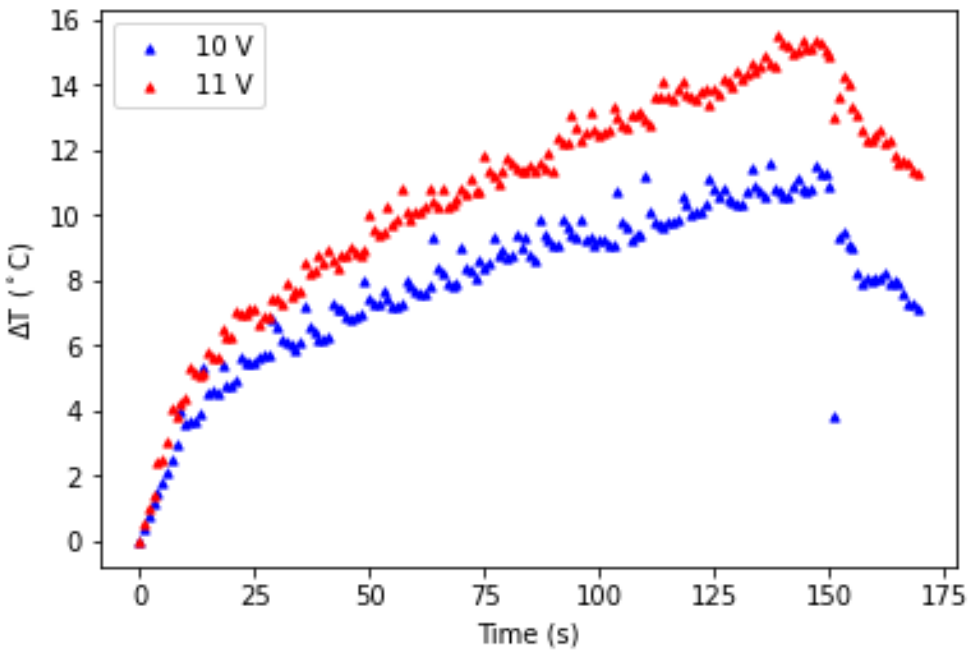

Figure 2.9 Temporal plot of ΔT for the device's hot spot. The liquid-metal droplet is injected into the well at the 150-s mark, rapidly cooling the hot spot in a short time frame. The cooling rate of the droplet can be determined if there was a larger sampling resolution after the 150-s mark. After the sudden temperature decrease, the hot-spot temperature transitions to a higher temperature because the droplet moves away from the hot spot and toward the heat sink.

Figure 2.10 shows the temperature data averaged over the entire 3 cm × 3 cm NaOH well [Figure 2.8(c) and Figure 2.8(d)], instead of just the hot spot. Each data point represents the average of four separate trials. As the hot spot continues to increase in temperature, the entire well increases in temperature. As in Figure 2.9, the temperature of the well decreases past the 150-s mark due to the liquid-metal droplet cooling the hot-spot region. In contrast to Figure 2.9, the results in Figure 2.10 show that between the 150-s and 175-s marks, there is a sudden temperature increase after hot spot cooling. This is most likely due to the overall device temperature being plotted instead of just examining the hot spot. As shown in Figure 2.9 and Figure 2.10, there are less data points around the temperature drop. Gathering more data points before the temperature drop can help determine the cooling rate of the liquid-metal droplet. Thus, further research must be performed to obtain a better resolution.

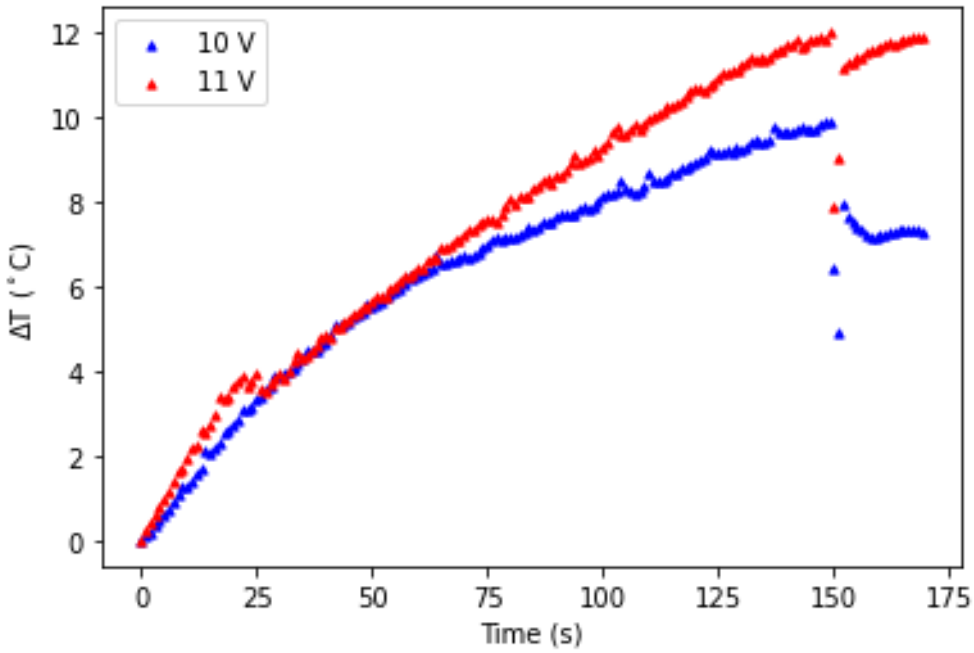

Figure 2.10 Temporal plot of ΔT for the NaOH well with the liquid-metal droplet injected at the 150-s mark.

2.2.4 Effects of NaOH Electrolyte on Joule Heating

A further investigation with Joule heating was performed by adjusting the NaOH molarity. By varying the molarity of the NaOH solution within the well, the NaOH conductivity can be controlled. In Figure 2.11, the change in temperature at the hot spot was measured for 1-M, 0.5-M, and 0.1-M NaOH. As the NaOH molarity increases, the NaOH conductivity should increase too. As shown in Figure 2.11, the result was expected because a higher electrical conductivity results in a higher thermal conductivity.

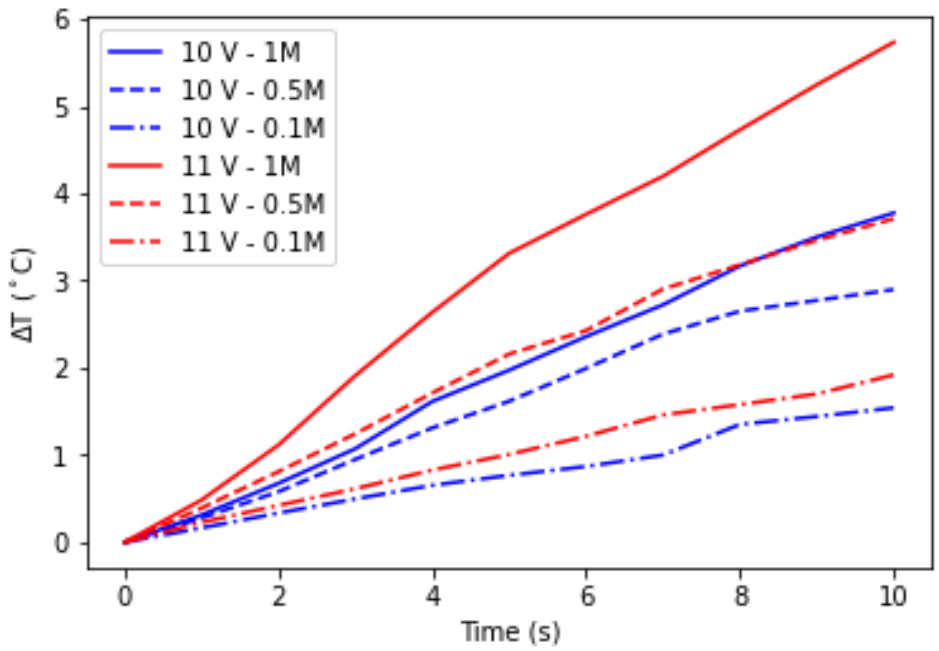

Figure 2.11 A temporal plot of ΔT for various NaOH molarities. The 1-M (solid), 0.5-M (dashed), and 0.1-M (dash-dotted) NaOH have varying rates of temperature change.

Since NaOH molarity affects the flow of electrical current from the electrodes through the NaOH and thus affects heat, several conclusions can be drawn for future device construction. Since any NaOH molarity is sufficient to perform CEW actuation of liquid metals, decreasing the NaOH molarity helps the device retain less heat from actuation, or when holding the liquid-metal droplet at a particular location. The draw-back of using a lower NaOH molarity, which is closer to a pure water solution, is that higher CEW actuation voltages are needed [38].

2.3 Conclusions

This chapter investigated the electrical actuation of a liquid-metal droplet along an arbitrarily prescribed two-dimensional path. Liquid-metal droplet actuation along straight-line and arbitrary paths within a two-dimensional plane have been demonstrated. Using the concept of two-dimensional actuation, rapid hot-spot cooling along a two-dimensional plane was also demonstrated. For an actuation voltage of 10 V DC, the liquid-metal droplet decreases the temperature of a localized hot spot by approximately 7 °C. Thermal effects of applied actuation voltages and variations in NaOH molarity have been quantified. Further improvements of this work, such as hot-spot

temperature reductions greater than 7 °C or decreasing the size of the device, will improve its potential for use in chip-cooling applications.

CHAPTER 3. ELECTROCAPILLARY ACTUATION OF LIQUID METAL IN MICROCHANNELS[2]

3.1 Introduction

In applications such as [14,15] and [18–22], the position or the physical dimensions of the liquid metal is altered via electrical actuation techniques that manipulate the liquid metal's surface tension. Compared to mechanically pressure-driven methods, electrical actuation is a relatively low power (typically milliwatts or less) [35] technique.

Liquid-metal motion in confined channels using electrical actuation was investigated in [35] and [40]. In [35], a quasi-planar reservoir was used to increase the liquid metal's sensitivity to an electrical actuation technique called electrocapillary actuation (ECA). In [40], finite volumes of liquid metal entered and exited a confined channel while under the influence of a DC electric field. Although both works demonstrated electrically-driven liquid metals in a confined environment, the device channel widths were 1 mm or larger. However, liquid metal could also be used in smaller channels for potential applications such as millimeter-wave wireless systems [4] or three-dimensional heterogeneous integration [33]. Thus, it is important to observe the dynamics of liquid metal in sub-millimeter-wide channels.

This chapter investigates ECA-activated liquid metal in channels with sub-millimeter widths. The results presented here will aid in designing devices that require liquid metal with characteristic dimensions in the microscale.

3.2 Materials and Methods

The microchannels used to characterize the liquid metal were fabricated in a layer of polydimethylsiloxane (PDMS) that was bonded to glass (Figure 3.1). The structure has inlet and outlet reservoirs at the ends of the device. Connecting these reservoirs are two channels of the same width w_0: a 2-cm-long primary channel that facilitates liquid metal flow and a 2.7-cm-long bypass channel to divert electrolytic fluid displaced by the liquid metal. The bypass channel is longer than

[2] The work presented in this chapter is based on: S. J. Dacuycuy, W. A. Shiroma, and A. T. Ohta, "Electrocapillary actuation of liquid metal in microchannels," *Micromachines*, vol. 13, no. 4, p. 572, 2022 [39].

the primary channel to increase its fluidic resistance and make the liquid metal flow preferentially into the primary channel. Both channels have a height of 100 µm.

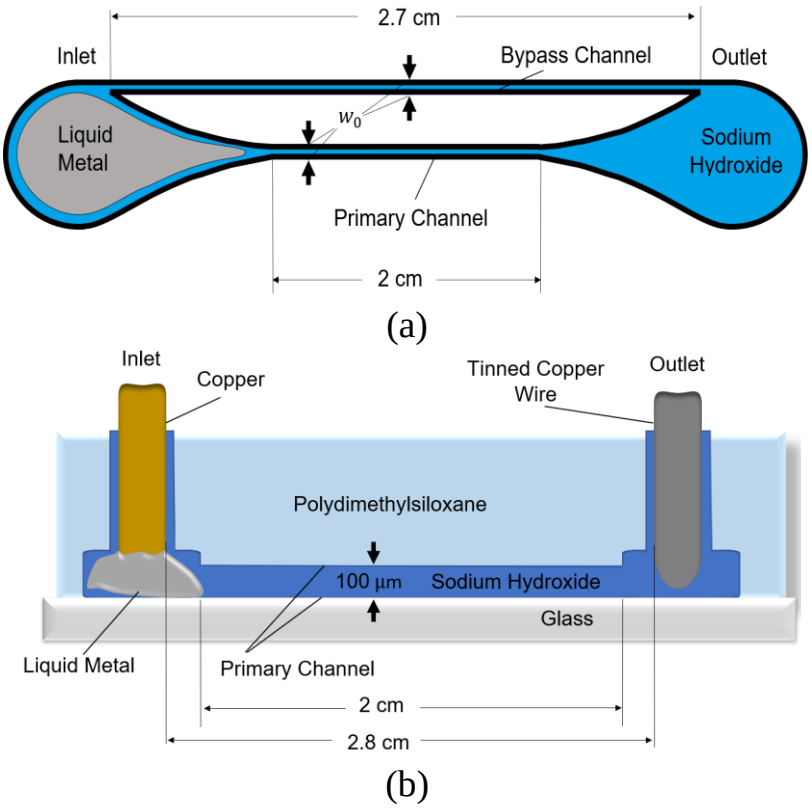

Figure 3.1 Layout of the microfluidic device for the electrocapillary actuation of liquid metal: (a) top view and (b) cross-sectional view.

The channels are filled with a 1 M sodium hydroxide (NaOH) solution, and the inlet reservoir contains Galinstan liquid metal. Gallium-based liquid metals form self-passivating oxide skins [41], which wet to many surfaces. The NaOH solution reduces the oxide layer around the liquid metal, which allows the liquid metal to behave like a liquid and respond to the ECA actuation signal.

Since liquid metal readily wets to copper, a copper rod was fixed in the inlet to serve as one electrode. As a result of liquid metal wetting to copper, the liquid metal is bound to the channel inlet. A 22-AWG tinned copper jumper wire was fixed in the outlet to serve as the second electrode; however, the outlet electrode could be made of any conductive material. The distance between the electrodes is 2.8 cm. An Arduino Mega ADK was used to control the ECA electrode voltage.

3.3 Concept

The concept is illustrated in Figure 3.2. If an actuation voltage V_{act} is not applied to the electrodes, the liquid metal is at rest in the inlet reservoir since it does not exert any pressure into the channels. Applying a positive voltage to the NaOH solution relative to the liquid metal creates surface-tension gradients and generates Marangoni forces F_{Mar}, allowing the liquid metal to deform and enter the channels. To induce flow into the channels, the pressure exerted by the liquid metal P_{LM} must exceed the channels' capillary pressure. This condition is met when V_{act} is above some critical voltage threshold V_{th}. Since the bypass channel is longer than the primary channel, the capillary resistance of the bypass channel, P'_{cap}, is larger than the resistance of the primary channel, P_{cap}. The liquid metal will move down the path of least resistance, which is the primary channel, when P_{LM} is greater than P_{cap}.

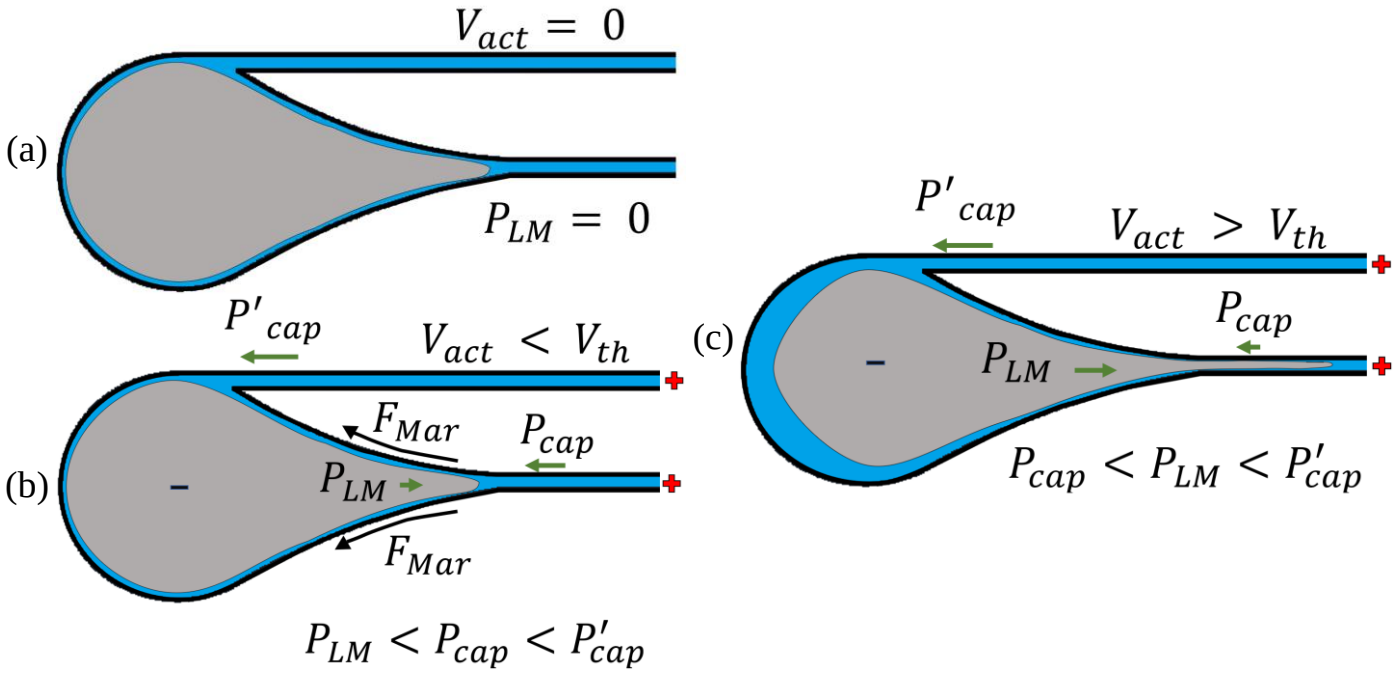

Figure 3.2 Electrocapillary actuation of liquid metal. (a) Liquid metal resting in an oval-shaped reservoir. (b) Applying a positive DC voltage (V_{act}) creates surface-tension gradients and Marangoni forces (F_{Mar}) at and near the surface of the liquid metal. The liquid metal now exerts a positive pressure (P_{LM}) on the channel entrances and opposes the channels' capillary pressure (P_{cap} and P'_{cap}). (c) Once the actuation voltage is above the voltage threshold V_{th}, the pressure exerted by the liquid metal exceeds the capillary pressure near the primary channel entrance. The bypass channel has a larger fluidic resistance, so the liquid metal preferentially flows into the primary channel.

Figure 3.3 illustrates the ECA mechanism. As the liquid metal enters and then travels down the primary channel, the liquid metal elongates within the channel. The arm length is defined as the displacement from the primary channel's entrance to the leading edge of the liquid metal.

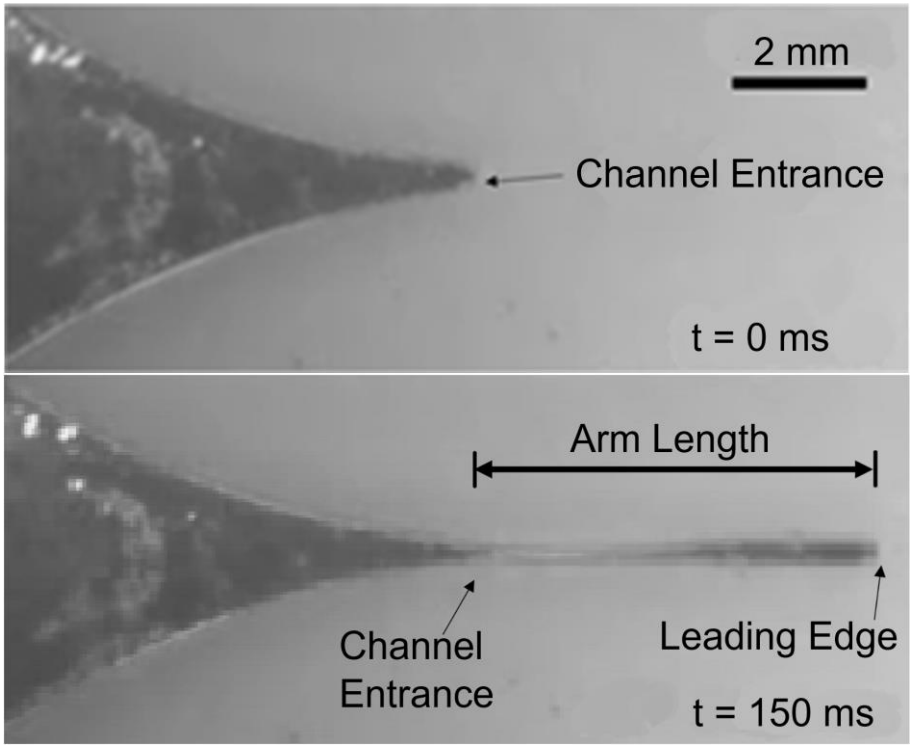

Figure 3.3 Liquid metal extending into the primary channel through ECA. (**a**) When there is no applied voltage, the liquid metal is resting at the channel entrance. (**b**) The liquid metal flowing in the primary channel. The displacement between the liquid-metal arm's leading edge and the channel entrance is measured to obtain the liquid-metal arm's length.

Figure 3.4 shows a time sequence for the liquid metal motion in a 200-μm-wide channel. In the following, we define the channel width as w_0 and the minimum width of the liquid-metal arm as w. Figure 3.4(a) shows the liquid metal at rest when no voltage is applied. Figure 3.4(b) shows a representative snapshot when the liquid metal has just entered the primary channel, where $w = w_0$. Figure 3.4(c) shows that as the liquid metal continues to elongate in the primary channel, w decreases such that $w < w_0$ at some point (usually near the primary channel entrance) until the liquid-metal arm breaks, as shown in Figure 3.4(d). The maximum arm length is defined as the longest arm length possible before the liquid-metal arm breaks.

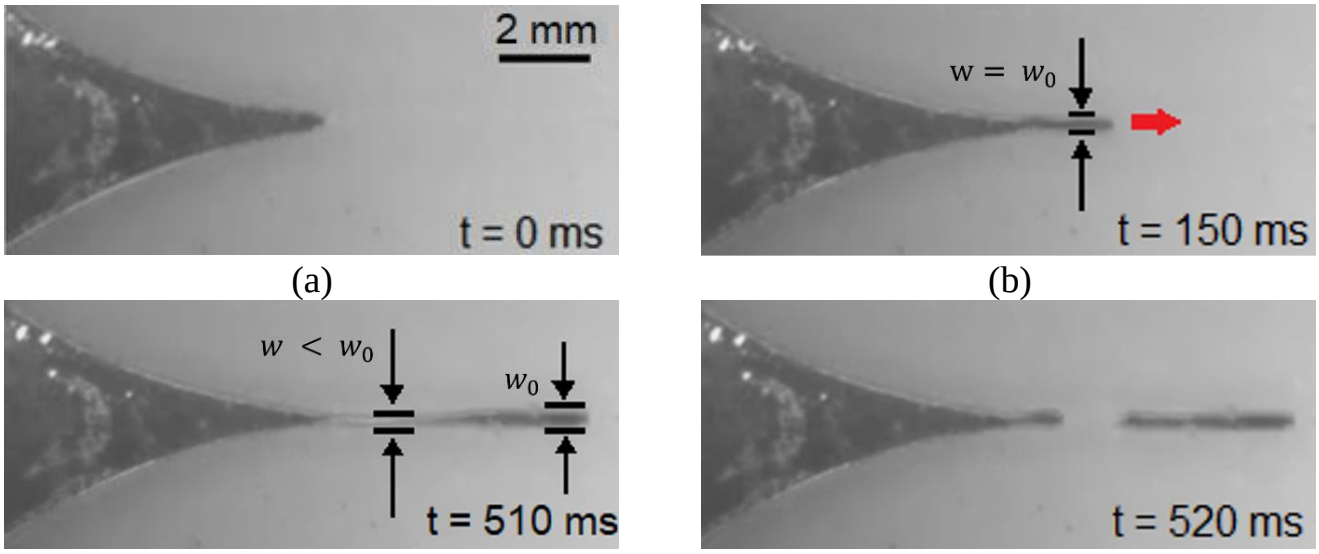

Figure 3.4 Demonstration of ECA for the liquid metal in a 200-μm-wide channel. (a) In the absence of an applied voltage, the liquid metal is initially at rest. (b) The liquid metal elongates and flows down the primary channel; this image is taken 150 ms after applying a positive 3 V DC bias. The width of the liquid-metal arm is approximately the same as the channel width. (c) At t = 510 ms, the width of the liquid-metal arm gets thinner near the channel entrance and is narrower than the width of the arm at the leading edge, which remains approximately the same as the channel width. (d) As the liquid metal moves down the primary channel, the liquid-metal arm breaks into discrete volumes, near the point at which the liquid-metal arm is thinnest.

3.4 Results and Discussion

3.4.1 Elongation of Liquid Metal

The average velocity of the liquid-metal arm as a function of actuation voltage was measured for four channel widths (Figure 3.5). The average velocity is found by measuring the displacement between the liquid metal at rest to the furthest point before it breaks, then dividing by the time it takes the liquid metal to travel that displacement. A data point in Figure 3.5 represents the mean of the average velocity for six trials.

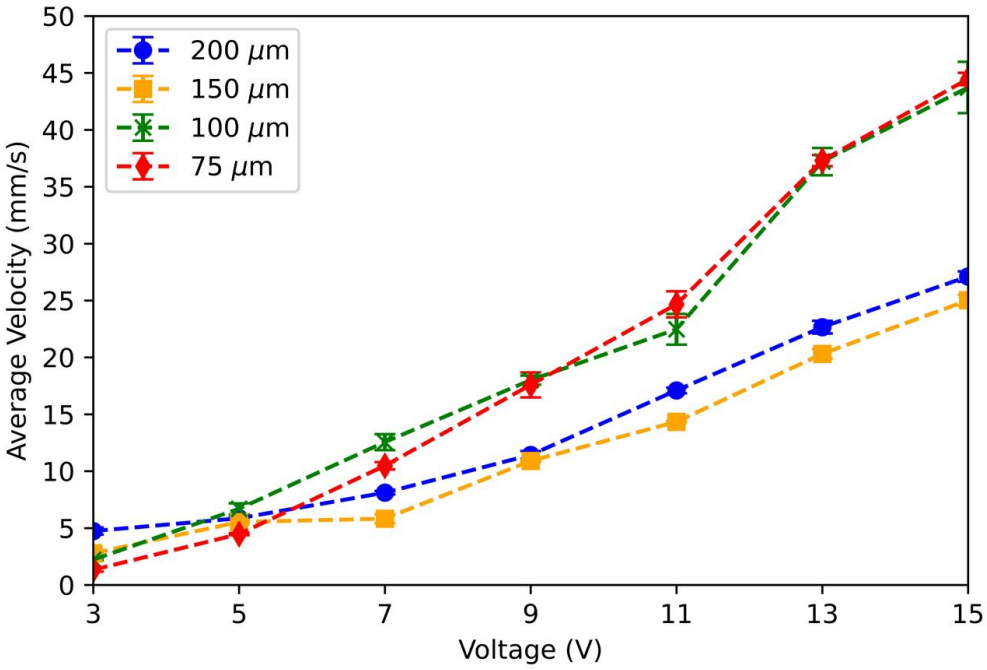

Figure 3.5 Average ECA velocity as a function of voltage. The narrower channels exhibit higher average velocities than the wider channels as the actuation voltage increases.

For all channels, the average velocity increases as the actuation voltage increases. The liquid metal in the narrower (75 μm and 100 μm) channels exhibit higher actuation velocities compared to liquid metal in the wider (150 μm and 200 μm) channels. For an actuation voltage of 15 V DC, liquid metal in the narrower channels has velocities approximately 1.7 times faster than in the wider channels. Intuitively, the average velocity should saturate as the actuation voltage increases, but the relationship is roughly linear for the voltages used in this experiment.

Figure 3.6 shows the maximum arm length as a function of voltage. Each data point represents the mean of the maximum arm lengths for six trials. The general trend shows that the maximum arm length decreases as the voltage increases. The likely reason for shorter maximum arm lengths at higher voltages is due to the instability of liquid metal during rapid deformation. When the actuation voltage is low and the liquid metal moves more slowly, the system is more mechanically stable, allowing the liquid metal to stretch to longer lengths. However, as shown in Figure 3.5, higher voltage causes the liquid metal to move more quickly, decreasing the system's stability. This likely explains why the liquid metal breaks at shorter arm lengths as the actuation voltage is increased.

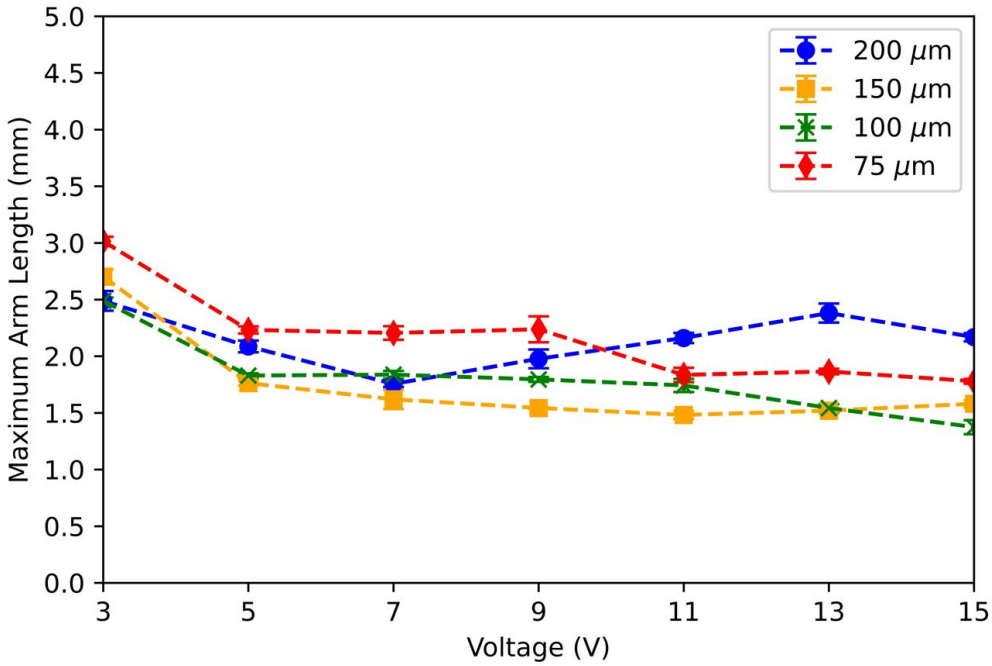

Figure 3.6 Maximum arm length as a function of voltage. The maximum arm length decreases slightly as the actuation voltage increases.

3.4.2 Occupation Ratio

To provide more insight into the liquid-metal breakup dynamics shown in Figure 3.4, we define the occupation ratio, $w/w_0 \times 100\%$. Figure 3.7 plots the measured occupation ratio as a function of the arm length. For this measurement, the actuation voltage was set at 3 V DC so that the liquid-metal arm could extend to its greatest length. Each data point represents the average of six trials, but the arm length was only averaged up to the shortest maximum arm length among the six trials. Thus, the end of the curves in Figure 3.7 may not have the same arm length value shown in Figure 3.6.

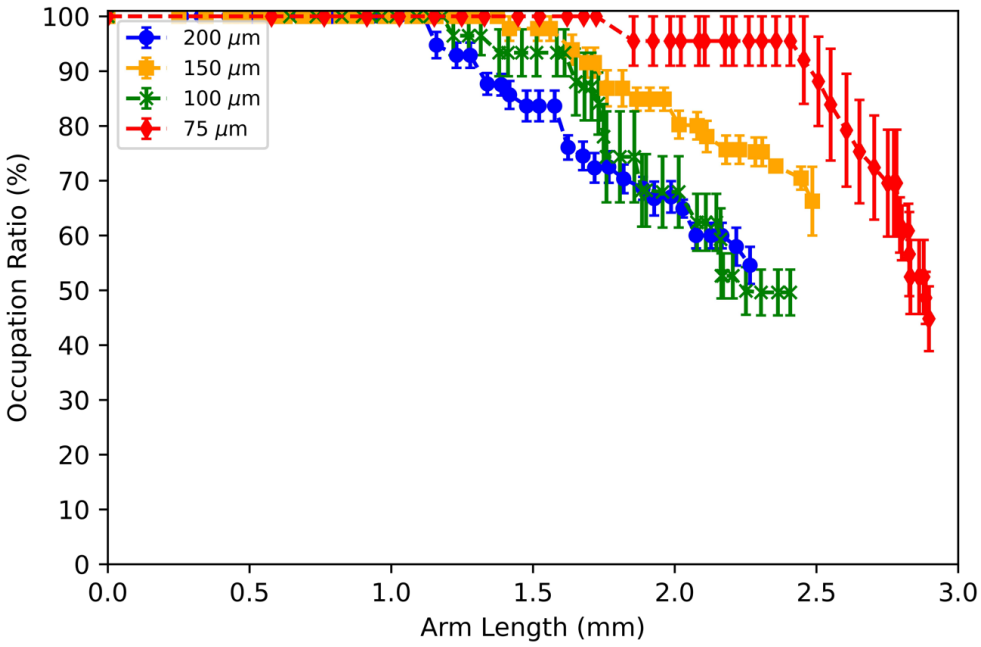

Figure 3.7 The occupation ratio, or the ratio between the liquid-metal arm's thinnest width to its respective channel width ($w/w_0 \times 100\%$), as a function of the arm length. For all channel widths, the liquid-metal arm retains an occupation ratio up to 100% at an arm length of 1 mm and can extend beyond an arm length of 2 mm before breaking. The actuation voltage is set at 3 V DC.

For all channel widths, the liquid-metal arm retains an occupation ratio of 100% up to an arm length of 1 mm (Figure 3.7). For all channel widths tested, the liquid metal's occupation ratio decreases between an arm length of 1 mm to 1.5 mm. The liquid metal's occupation ratio then decreases by 40% per mm, regardless of the channel width. This shows that the liquid-metal arm for all channel widths can undergo sizable deformation before reaching its breaking point.

If the liquid-metal arm breaks apart during ECA, the voltage polarity can be switched to return the broken segment of liquid metal into the inlet reservoir. The ability to return the liquid metal back to its original state suggests that the device can be used multiple times.

The instantaneous velocity at the liquid-metal arm's leading edge was also measured when a 3-V DC ECA voltage was applied (Figure 3.8). The arm length was observed up to 2 mm since the liquid metal in all channels remains unbroken at this arm length. Like Figure 3.7, a data point in Figure 3.8 represents the average of six trials, except the arm length was averaged only up to the shortest maximum arm length among the six trials.

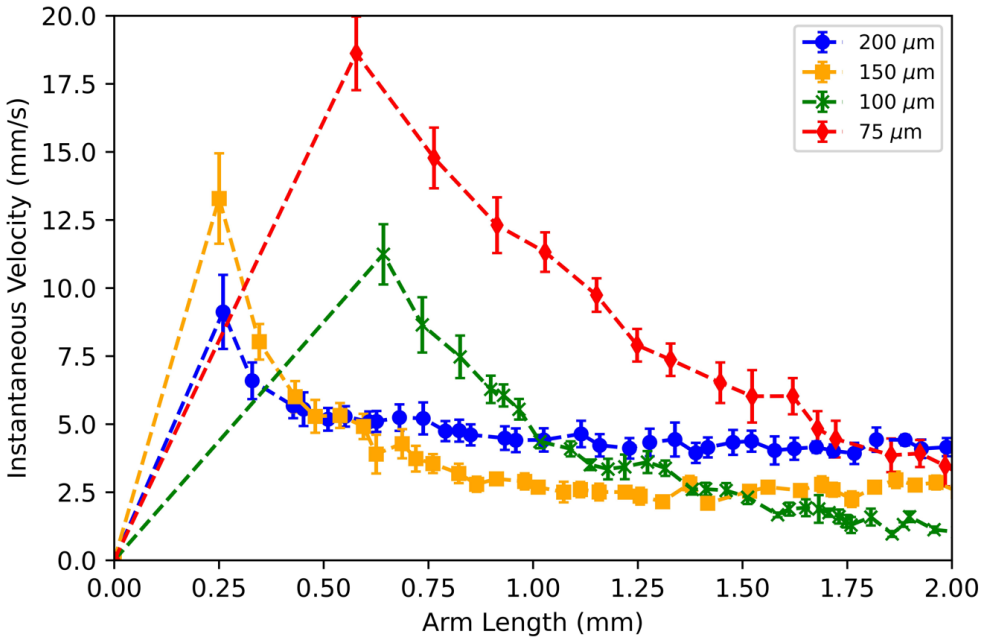

Figure 3.8 Measured ECA actuation velocities for an actuation voltage of 3 V DC. For all channel widths, as the liquid-metal arm increases, the instantaneous velocity reaches a maximum value and gradually decreases.

For all channel widths, as the liquid-metal arm increases, the instantaneous velocity reaches a maximum value and then gradually decreases, showing that the instantaneous velocity is not constant as the liquid metal moves down the channel.

3.5 Conclusions

In summary, this chapter characterizes the deformation of liquid metal in microchannels due to ECA. The dynamics and the physical limitations of actuated liquid metal were observed for a voltage range of 3 V DC to 15 V DC. At an actuation voltage of 3 V DC, the liquid-metal arm could extend more than 2.5 mm into the channel. Although the results presented here were specific to a 2-cm long channel, the results could be generalized for channels of other lengths by converting the ordinate axes of Figures 3.5 and 3.6 to an electric field, which is the actuation voltage divided by the distance between the electrodes (2.8 cm). The results presented from this research will aid in the design of microdevices that use electrically actuated liquid metal, such as biomedical devices and sub-millimeter systems that require reconfigurable and tunable metal elements. For

example, the deformation of liquid metal at these small volumes could be used in millimeter-wave systems. Adjusting the length of a liquid-metal arm could be used to create a tunable load-matching transmission line stub.

CHAPTER 4. CONCLUSIONS AND FUTURE WORK

4.1 Conclusions

This research was motivated by the need for using small volumes of liquid metal as an innovative solution. In this work, two devices using liquid metal as a functional material were fabricated and tested for applications in thermal management and microfluidics. Specifically, this research was intended to diversify the role of liquid metal into new avenues of research by acting as a reconfigurable and tunable metal element.

In Chapter 2, CEW is used to actuate a liquid-metal droplet along a two-dimensional plane. Through the dynamic movement of a liquid-metal droplet, rapid hot-spot cooling can be achieved for an arbitrarily located hot spot. In Chapter 3, ECA actuation is used to perform controlled deformation of liquid metal in microchannels. This research can potentially be used in applications that require reconfigurable metallic elements at the sub-millimeter-length scale.

4.2 Future Work

4.2.1 Higher Resolution at Hot-Spot Cooling

Additional data collection is required as there are less data points around the temperature drop, as shown in Figure 2.9 and Figure 2.10. Gathering more data points before and after the temperature drop can help provide an accurate representation of the hot-spot cooling phenomenon. Finding data points before the temperature drop can help determine the cooling rate of the liquid-metal droplet. Obtaining points after the temperature drop could help determine whether the sustained heat from the activated electrode can overcome the cooling effect of the liquid-metal droplet.

4.2.2 Continuous Pumping of Liquid-Metal Droplets for Hot-Spot Cooling

The research presented in Chapter 2 is a proof-of-concept. The scientific merit of this research could be expanded with a discussion of the implications describing the cooling capacity of a liquid-metal droplet. The next step would be to demonstrate the pumping power of the device by moving the droplet back and forth to create a “bucket brigade” of liquid-metal droplet cooling (Figure 4.1).

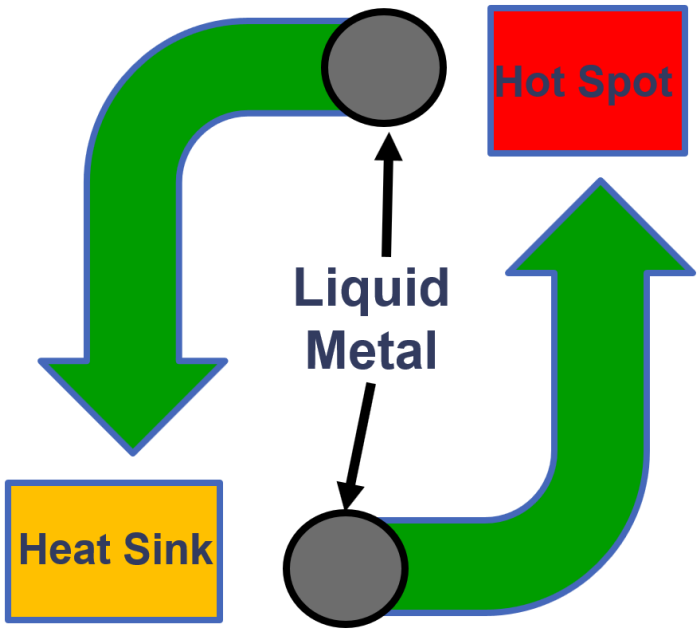

Figure 4.1 Concept of a liquid-metal bucket brigade. A liquid-metal droplet is actuated back and forth between the hot spot and heat sink to demonstrate continuous pumping of heat on the hot spot.

This approach could effectively pump heat in a continuous fashion rather than temporarily lowering the temperature of the hot spot.

4.2.3 Further Investigation of Occupation Ratio

The research presented in Chapter 3 could be extended by analyzing the occupation ratios of the liquid metal for actuation voltages greater than 3 V DC. The work shown in Section 3.4.2 has the actuation voltage set at 3 V DC so that the liquid metal arm could extend to its greatest length. However, it would be useful to include a further analysis of Figure 3.7 and Figure 3.8 with a voltage range from 3 V DC to 15 V DC. Including this analysis for higher actuation voltages could give an accurate characterization of liquid metal in sub-millimeter-wide channels.

4.2.4 Improvements on Fabrication and Design

The work done in this thesis includes the design of two types of devices meant for actuating liquid metal. For the actuation device in Chapter 2, improvements can be made by fabricating the well to be larger than 3 cm × 3 cm × 0.8 cm. Having a larger well allows for better spacing between the electrodes and avoids coupling when the electrodes are activated. The operation of the

microfluidic channels in Chapter 3 can be optimized by fabricating the bypass channel's length beyond 2.7 cm. For actuation voltages greater than 3 V DC, the liquid metal can enter both the primary and bypass channels when performing ECA. This occurs because the pressure exerted by the liquid metal exceeds both channels' capillary pressure. Thus, for all actuation voltages, the bypass channel's fluidic resistance should be greater than the pressure exerted by liquid metal.

REFERENCES

[1] J. Kahn, “Startup Graphcore aims to displace Nvidia with new computer chips,” *Fortune*, 15-Jul-2020. [Online]. Available: https://fortune.com/2020/07/15/startup-graphcore-takes-on-nvidia-with-latest-a-i-chip/. [Accessed: 12-Apr-2022].

[2] T. Li, Y.-G. Lv, J. Liu, and Y.-X. Zhou, “A powerful way of cooling computer chip using liquid metal with low melting point as the cooling fluid,” *Forschung im Ingenieurwesen*, vol. 70, no. 4, pp. 243–251, 2006.

[3] Z. Zhang, Y. Xiao, Z. Ma, M. Xiao, Z. Ding, X. Lei, G. K. Karagiannidis, and P. Fan, “6G wireless networks: Vision, requirements, architecture, and Key Technologies,” *IEEE Vehicular Technology Magazine*, vol. 14, no. 3, pp. 28–41, 2019.

[4] S. Zhang, J. Liu, H. Guo, M. Qi, and N. Kato, “Envisioning device-to-device communications in 6G,” *IEEE Netw.*, vol. 34, no. 3, pp. 86–91, 2020.

[5] J. M. Rabaey, A. Chandrakasan, and B. Nikolic, *Digital Integrated Circuits: A Design Perspective*, 3rd ed. Upper Saddle River, NJ: Prentice Hall Press, 2008.

[6] G. Xu, “Evaluation of a liquid cooling concept for high power processors,” in *Proc. IEEE Semicond. Therm. Meas. Manage. Symp.*, Mar. 2014, pp. 190–195.

[7] J. Mao, G. Chen, and Z. Ren, “Thermoelectric cooling materials,” *Nature Materials*, vol. 20, no. 4, pp. 454–461, 2020.

[8] F. M. Wisser, B. Schumm, G. Mondin, J. Grothe, and S. Kaskel, “Precursor strategies for metallic nano- and micropatterns using soft lithography,” *Journal of Materials Chemistry C*, vol. 3, no. 12, pp. 2717–2731, 2015.

[9] Y. Sui and C. A. Zorman, “Review—inkjet printing of metal structures for Electrochemical Sensor Applications,” *Journal of The Electrochemical Society*, vol. 167, no. 3, p. 037571, 2020.

[10] K. Koshmanesh, S.-Y. Tang, J. Y. Zhu, S. Schafer, A. Mitchell, K. Kalantar-zadeh, and M.

D. Dickey, “Liquid metal enabled microfluidics,” *Lab Chip*, vol. 17, no. 6, pp. 974–993, 2017.

[11] J. Liu, L. Sheng, and Z.-Z. He, *Liquid Metal Soft Machines*, 1st ed. Singapore: Springer, 2019.

[12] S. Park and H.-J. Yoon, “New approach for large-area thermoelectric junctions with a liquid eutectic gallium-indium electrode,” *Nano Lett.*, vol. 18, no. 12, pp. 7715–7718, 2018.

[13] K. Y. Alqurashi, J. R. Kelly, Z. Wang, C. Crean, R. Mittra, M. Khalily, and Y. Gao, “Liquid metal bandwidth-reconfigurable antenna,” *IEEE Antennas Wirel. Propag. Lett.*, vol. 19, no. 1, pp. 218–222, 2020.

[14] R. C. Gough, J. H. Dang, A. M. Morishita, A. T. Ohta, and W. A. Shiroma, “Frequency-tunable slot antenna using continuous electrowetting of liquid metal,” in *Proc. IEEE MTT-S Int. Microwave Symp. (IMS 2014)*, Jun. 2014, pp. 1–4.

[15] M. Wang, C. Trlica, M. R. Khan, M. D. Dickey, and J. J. Adams, “A reconfigurable liquid metal antenna driven by electrochemically controlled capillarity,” *J. Appl. Phys.*, vol. 117, no. 19, p. 194901, 2015.

[16] K. Peng, J. Yao, S. Cho, Y. Cho, H. S. Kim, and J. Park, “Liquid metal embedded real time microfluidic flow pressure monitoring sensor,” *Sens. Actuators A*, vol. 305, p. 111909, 2020.

[17] M. Varga, C. Ladd, S. Ma, J. Holbery, and G. Tröster, “On-skin liquid metal inertial sensor,” *Lab Chip*, vol. 17, no. 9, pp. 3272–3278, 2017.

[18] S. J. Dacuycuy, W. A. Shiroma, and A. T. Ohta, “Two-dimensional actuation of liquid-metal droplets for hot-spot cooling,” in *Proc. IEEE Intersociety Conf. Therm. and Thermomech. Phenom. Electron. Syst. (iTherm)*, Jun. 2021, pp. 1262–1267.

[19] T. Yang, B. Kwon, P. B. Weisensee, J. G. Kang, X. Li, P. Braun, N. Miljkovic, and W. P. King, “Millimeter-scale liquid metal droplet thermal switch,” *Appl. Phys. Lett.*, vol. 112, no. 6, p. 063505, 2018.

[20] J. Y. Zhu, S.-Y. Tang, K. Khoshmanesh, and K. Ghorbani, "An integrated liquid cooling system based on Galinstan liquid metal droplets," *ACS Appl. Mater. Interfaces*, vol. 8, no.3, pp. 2173–2180, 2015.

[21] J. Y. Zhu, P. Thurgood, N. Nguyen, K. Ghorbani, and K. Khoshmanesh, "Customised spatiotemporal temperature gradients created by a liquid metal enabled vortex generator," *Lab Chip*, vol. 17, no.22, 2017.

[22] S.-Y. Tang, K. Khoshmanesh, V. Sivan, and K. Kalantar-zadeh, "Liquid metal enabled pump," *Proc. Natl. Acad. Sci. USA*, vol. 111, no. 9, pp. 3304–3309, 2014.

[23] R. C. Chiechi, E. A. Weiss, M. D. Dickey, and G. M. Whitesides, "Eutectic gallium–indium (EGaIn): A moldable liquid metal for electrical characterization of self-assembled monolayers," *Angew. Chem. Int. Ed.*, vol. 47, no. 1, pp. 142–144, 2007.

[24] F. C. Simeone, H.-J. Yoon, M. M. Thuo, J. R. Barber, B. Smith, and G. M. Whitesides, "Defining the value of injection current and effective electrical contact area for EGaIn-based molecular tunneling junctions," *J. Am. Chem. Soc.*, vol. 135, no. 48, pp. 18131–18144, 2013.

[25] S. Park, S. Kang, and H.-J. Yoon, "Power factor of one molecule thick films and length dependence," *ACS Cent. Sci.*, vol. 5, no. 12, pp. 1975–1982, 2019.

[26] H. Song, T. Kim, S. Kang, H. Jin, K. Lee, and H.-J. Yoon, "Ga-based liquid metal micro/nanoparticles: Recent advances and applications," *Small*, vol. 16, no. 12, p. 1903391, 2019.

[27] J. Wang, S. Liu, Z.-V. Vardeny, and A. Nahata, "Liquid metal-based plasmonics," *Opt Express*, vol. 20, no. 3, pp. 2346–2353, 2012.

[28] K. Zuraiqi, A. Zavabeti, F.-M. Allioux, J. Tang, C. K. Nguyen, P. Tafazolymotie, M. Mayyas, A. V. Ramarao, M. Spencer, K. Shah, C. F. McConville, K. Kalantar-Zadeh, K. Chiang and T. Daeneke, "Liquid metals in catalysis for energy applications," *Joule*, vol .4, no. 11, pp. 2290–2321, 2020.

[29] C. B. Eaker and M. D. Dickey, “Liquid metal actuation by electrical control of interfacial tension,” *Appl. Phys. Rev.*, vol. 3, no. 3, p. 031103, 2016.

[30] S.-Y. Tang, V. Sivan, P. Petersen, W. Zhang, P. D. Morrison, K. Kalantar-zadeh, A. Mitchell, and K. Khoshmanesh, “Liquid metal actuator for inducing chaotic advection,” *Adv. Funct. Mater.*, vol. 24, no. 37, pp.5851–5858.

[31] X. Li, S. Li, Y. Lu, M. Liu, F. Li, H. Yang, S.-Y. Tang, S. Zhang, W. Li, and L. Sun, “Programmable digital liquid metal droplets in reconfigurable magnetic fields,” *ACS Appl. Mater. Interfaces*, vol. 12, no. 33, pp. 37670–37679, 2020.

[32] Z. Yan, M. Jin, Z. Li, G. Zhou, and L. Shui, “Droplet-based microfluidic thermal management methods for high performance electronic devices,” *Micromachines*, vol. 10, no. 2:89, 2019.

[33] J. P. Gambino, S. A. Adderly, and J. U. Knickerbocker, “An overview of through-silicon-via technology and manufacturing challenges,” *Microelectron. Eng.*, vol. 135, pp. 73–106, 2015.

[34] J. Lee and C.-J. Kim, “Surface-tension-driven microactuation based on continuous electrowetting,” *J. Microelectromech. Syst.*, vol. 9, no. 2, pp. 171–180, 2000.

[35] R. C. Gough, A. M. Morishita, J. H. Dang, M. R. Moorefield, W. A. Shiroma, and A. T. Ohta, “Rapid electrocapillary deformation of liquid metal with reversible shape retention,”, *Micro Nano Syst. Lett.*, vol. 3, no. 1, pp. 1–9, 2015.

[36] R. C. Gough, A. M. Morishita, J. H. Dang, W. Hu, W. A. Shiroma, and A. T. Ohta, “Continuous electrowetting of non-toxic liquid metal for RF applications,” *IEEE Access*, vol. 2, pp. 874–882, 2014.

[37] D. Brown, R. Hanson, and W. Christian, *Tracker Video Analysis and Modeling Tool for Physics Education*. [Online]. Avaialble: https://physlets.org/tracker/. [Accessed: 14-Dec-2020].

[38] L. Sheng, J. Zhang, and J. Liu, “Diverse transformation of liquid metals between different

morphologies," *Adv. Mater.*, vol. 26, no. 34, pp. 6036–6042, 2014.

[39] S. J. Dacuycuy, W. A. Shiroma, and A. T. Ohta, "Electrocapillary actuation of liquid metal in microchannels," *Micromachines*, vol. 13, no. 4, p. 572, 2022.

[40] D. Wang, Z. Lin, C. Zho, C. Gao, and Q. He, "Liquid metal gallium micromachines speed up in confining channels," *Adv. Intell. Syst.*, vol. 1, no. 7, p. 1970070, 2019.

[41] T. Liu, P. Sen, and C.-J. Kim, "Characterization of nontoxic liquid-metal alloy Galinstan for applications in microdevices," *J. Microelectromech. Syst.*, vol. 21, no. 2, pp. 443–450, 2012.